Dalton Transactions

ROYAL SOCIETY OF CHEMISTRY

PAPER

View Article Online
View Journal | View Issue



Check for updates

Cite this: *Dalton Trans.*, 2023, **52**, 9026

# Potassium-rich antiperovskites $K_3HTe$ and $K_3FTe$ and their structural relation to lithium and sodium counterparts†

Koji Okada, [a] Susumu Fujii, [b,c] Cédric Tassel,*[a] Shenghan Gao,[a] Hiroki Ubukata, [a] Wenli Pan,[d] Kentaro Yamamoto, [d,e] Yoshiharu Uchimoto, [d] Akihide Kuwabara *[b] and Hiroshi Kageyama *[a]

Received 5th April 2023,
Accepted 25th May 2023

DOI: 10.1039/d3dt01039b

rsc.li/dalton

Unlike perovskite oxides, antiperovskites $M_3HCh$ and $M_3FCh$ (M = Li, Na; Ch = S, Se, Te) mostly retain their ideal cubic structure over a wide range of compositions owing to anionic size flexibility and low-energy phonon modes that promote their ionic conductivity. In this study, we show the synthesis of potassium-based antiperovskites $K_3HTe$ and $K_3FTe$ and discuss the structural features in comparison with lithium and sodium analogues. It is shown experimentally and theoretically that both compounds maintain a cubic symmetry and can be prepared at ambient pressure, in contrast to most of the reported $M_3HCh$ and $M_3FCh$ which require high pressure synthesis. A systematic comparison of a series of cubic $M_3HTe$ and $M_3FTe$ (M = Li, Na, K) revealed that telluride anions contract in the order of K, Na, Li, with a pronounced contraction in the Li system. This result can be understood in terms of the difference in charge density of alkali metal ions as well as the size flexibility of Ch anions, contributing to the stability of the cubic symmetry.

## Introduction

Antiperovskites, represented by the chemical formula $X_3BA$ (A, B: anions, X: cations), exhibit diverse physical and chemical properties owing to a versatile array of chemical compositions (Fig. 1).[1–9] For example, lithium- and sodium-rich antiperovskites such as $M_3O(Cl_{1-x}Br_x)$ (M = Li, Na) exhibit excellent lithium/sodium ion conductivity that could be used in solid electrolytes for high energy density batteries.[1–3] Recently, we have synthesized antiperovskites $M_3HCh$ (M = Li, Na; Ch = S, Se, Te) with H anions at the B-site using high pressure reactions, and observed that the size flexibility of the $H^-$ anion stabilizes the ideal cubic structure ($Pm\bar{3}m$) over a wide compositional space, with the exception of $Na_3HS$.[10] These compounds show a high ionic conductivity, which can be attributed to the low energy phonon modes associated with the rotation of $HM_6$ octahedra, lowering the migration barrier for lithium and sodium cations.[10]

Subsequently, antiperovskites $M_3FCh$ (M = Li, Na; Ch = S, Se, Te) were synthesized mainly using the high pressure technique.[11] Despite the use of the hard F anion instead of the soft H anion, $M_3FCh$ also adopts the cubic structure with the

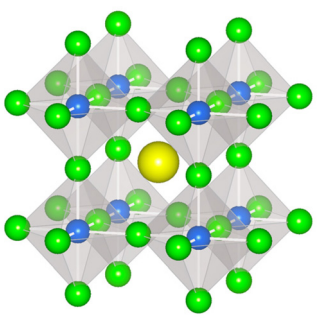

**Fig. 1** Crystal structure of alkali metal rich antiperovskite $M_3BTe$ (M = Li, Na, K; B = H, F). The newly synthesized $K_3HTe$ and $K_3FTe$ adopt the cubic symmetry ($Pm\bar{3}m$). The B-site anion (H or F) (blue) occupies the octahedral center formed by K cations (green) and the A-site telluride anion (yellow) occupies the cuboctahedral site.

[a]*Department of Energy and Hydrocarbon Chemistry, Graduate School of Engineering, Kyoto University, Nishikyo-ku, Kyoto 615-8510, Japan*
[b]*Nanostructures Research Laboratory, Japan Fine Ceramics Center, Nagoya 456-8587, Japan*
[c]*Division of Materials and Manufacturing Science, Graduate School of Engineering, Osaka University, Osaka 565-0871, Japan*
[d]*Graduate School of Human and Environment Studies, Kyoto University, Sakyo-ku, Kyoto 606-8501, Japan*
[e]*Faculty of Engineering, Nara Women's University, Kitauoyanishimachi, Nara 630-8506, Japan*

†Electronic supplementary information (ESI) available: Laboratory X-ray diffraction patterns of $K_3HTe$ and $K_3FTe$, size-flexibility of soft anions in other compounds, migration barriers in $K_3HTe$ and $K_3FTe$, and measured ionic conduction of pristine and iodine substituted $K_3HTe$ (PDF). See DOI: **https://doi.org/10.1039/d3dt01039b**

exception of $Na_3FS$, and thus comparable ionic conduction is obtained due to the associated low energy $FM_6$ octahedral rotation modes. These results, together with first-principles calculations, imply that highly polarizable Ch anions play a major role in stabilizing the cubic symmetry. Furthermore, we found a correlation between the soft phonon modes, the tolerance factor,[12] and the activation energy for the mobile cations.

This work aims to expand the available compositional space of $M_3HCh$ and $M_3FCh$ by including potassium instead of Li and Na. We have successfully synthesized $K_3HTe$ and $K_3FTe$ under both high pressure and ambient pressure conditions. The preparation of a series of alkali metal-rich antiperovskites allows us to compare them systematically together with first-principles calculations. It is found that in $M_3BCh$ (M = Li, Na, K; B = H, F; Ch = S, Se, Te), not only the size-flexibility of the Ch-site anions but also the charge density of the M-site cations has an impact on their structures.

## Experimental

Polycrystalline samples of $K_3HTe$ and $K_3FTe$ were initially synthesized by a solid-state reaction under high pressure using washed KH (Sigma-Aldrich, 30 wt% dispersion mineral oil) with hexane and $K_2Te$ (Kojundo, 99%), and KF (Wako, 99.0%) and $K_2Te$ as precursors, respectively. $K_3FTe$ was obtained with a stoichiometric ratio (*i.e.*, $KF : K_2Te = 1 : 1$), while the synthesis of $K_3HTe$ requires a hydrogen-rich ratio of $KH : K_2Te = 2 : 1$, as is the case with other oxyhydrides synthesized under pressure including $SrCrO_2H$,[13] $BaScO_2H$,[14] $BaVO_{3-x}H_x$ ($0.3 \leq x \leq 0.8$)[15] and $LaSrMnO_{3.3}H_{0.7}$.[16] The starting materials were thoroughly ground and pressed into a pellet, which was inserted into a boron nitride (BN) sleeve and sealed at both ends with BN caps. The assembly was then loaded into a graphite tube heater and sealed in a pyrophyllite cube, serving as a pressure medium. All the above procedures were conducted in a glovebox filled with $N_2$ (mBRAUN, Unilab-2000) due to the instability of the precursors and the products towards air and humidity. The cubic cells were pressed under 5 GPa, and then heated at 400 °C for 10 min for $K_3HTe$ and at 750 °C for 10 min for $K_3FTe$. After maintaining the temperature for 1 hour, the samples were cooled to room temperature in 5 min before the pressure was released. The recovered cells were placed back in the glovebox and the obtained polycrystalline samples were collected. We also attempted to synthesize both compounds under ambient pressure; pellets of the mixture of starting materials were vacuum sealed into Pyrex tubes and heated at 330 °C for 14 hours for $K_3HTe$ and at 450 °C for 14 hours for $K_3FTe$. Iodine-substituted $K_3HTe$ was synthesized using a mixture of KH, $K_2Te$ and KI with a hydrogen-rich ratio of $2 : 0.9 : 0.1$ under the same conditions as those for pristine $K_3HTe$.

High-resolution synchrotron X-ray diffraction (SXRD) measurements were carried out at room temperature with a wavelength of $\lambda = 0.42$ Å at the BL02B2 beamline in SPring-8 (Japan), equipped with MYTHEN solid-state detectors. The $K_3HTe$ and $K_3FTe$ powder samples were sealed in borosilicate capillaries. Le Bail and Rietveld analyses of SXRD data were carried out using JANA2006 software,[17] while the crystal structures were visualized using VESTA.[18]

Ionic conductivities of cold-pressed pellets of $K_3HTe$ and I-substituted $K_3HTe$ were measured by electrochemical impedance spectroscopy (EIS) with a constant voltage of 10 mV in the frequency range from 1 MHz to 0.1 Hz using an ECS ModuLab potentiostat/galvanostat. Around 0.2 g of the powder specimen was placed between two stainless-steel rods as an ion-blocking electrode in a custom-made Swagelok cell and pressed into a 10 mm diameter pellet using a hydraulic press at 360 MPa (thickness: 1–1.5 mm). The temperature was varied from 25 °C to 100 °C. Data at each temperature were collected after being held for 115 min to ensure temperature stabilization.

*Ab initio* calculations on $K_3HTe$, $K_3FTe$, KH, KF and $K_2Te$ were performed under 0 and 5 GPa using the plane-wave basis projector augmented wave (PAW) method[19] implemented in the Vienna *Ab initio* Simulation Package (VASP).[20,21] The generalized gradient approximation in the form of PBEsol[22] was employed. The valence configurations in the PAW potentials used in this study are as follows: [$3s^2$ $3p^6$ $4s^1$] for K, [$1s^1$] for H, [$2s^2$ $2p^5$] for F, and [$5s^2$ $5p^4$] for Te. The remaining electrons were treated as frozen core electrons. The plane-wave energy cutoff was set to 650 eV. The first Brillouin zone was sampled using Γ-centered *k*-point grids with a spacing of 0.2 $Å^{-1}$. The total energy convergence was set to $1.0 \times 10^{-6}$ eV per atom, and atomic positions and lattice constants were relaxed until the residual forces of atoms were less than $1.0 \times 10^{-3}$ eV $Å^{-1}$.

Phonon band structures and vibrational free energies under harmonic approximation were calculated using the finite displacement method[23] implemented in Phonopy.[24] The displacement of atoms from their stationary positions to obtain second-order force constants was set to 0.01 Å. A $2 \times 2 \times 2$ supercell with respect to the conventional unit cell was used to avoid the self-interaction between the displaced atoms. Non-analytical term correction[25] was adopted using the Born effective charge tensors and dielectric constants calculated using density functional perturbation theory implemented in VASP.[20,21]

The nudged elastic band (NEB) method[26] was used to calculate the energy barriers of $K^+$ migration *via* vacancies and interstitial defects (dumbbell) in $K_3HTe$ and $K_3FTe$. Charged supercells with the dimensions of $3 \times 3 \times 3$ were used. The first Brillouin zone was sampled with one *k*-point (0.25, 0.25, 0.25) due to the large size of supercells. For NEB calculations, the total energy and force convergence were set to $1.0 \times 10^{-6}$ eV per cell and $2.0 \times 10^{-2}$ eV $Å^{-1}$, respectively. Note that all the computational conditions employed here are consistent with our previous studies.[10,11]

## Results and discussion

As shown in Fig. S1a,† the XRD pattern of $K_3HTe$ synthesized at 400 °C under 5 GPa is similar to that of the ideal antiperovs-

kite $Na_3HTe$ ($Pm\bar{3}m$).[10] Several additional reflections were assigned to unreacted KH, while the remaining small peaks could not be assigned to any known phases, nor to a superstructure as found in $Na_3HS$ and $Na_3FS$ with coherent octahedral rotations.[10,11] The lattice parameter of $K_3HTe$, $a$ = 5.35927(2) Å, is longer than that of $Na_3HTe$ ($a$ = 4.76349(2) Å),[10] reflecting the difference in ionic radius between Na and K ($Na^+$: 1.02 Å *vs.* $K^+$: 1.38 Å).[27] Similarly, the XRD pattern of $K_3FTe$ was indexed in the ideal cubic structure, along with KF and unknown impurities (Fig. S1b†). The lattice constant $a$ = 5.25451(1) Å is longer than that of the Na counterpart ($a$ = 4.70315(1) Å).[11]

Rietveld refinement of the SXRD data for $K_3HTe$ assuming the cubic antiperovskite structure ($Pm\bar{3}m$) readily converged to $GOF$ = 3.94, $R_p$ = 5.44% and $R_{wp}$ = 7.56% (Fig. 2a), with reasonable isotropic atomic displacement parameter, $U_{iso}$, values of 0.0385(2) $Å^2$ and 0.0239(1) $Å^2$ for K and Te, respectively. Refining occupancy factors, $g$, at K resulted in 0.988(1). Note that the $U_{iso}$ of H and $g$ of H and Te are not refined. Likewise, the Rietveld analysis of $K_3FTe$ converged successfully, yielding $GOF$ = 5.52, $R_p$ = 5.33% and $R_{wp}$ = 7.31%, $U_{iso}$ of 0.0235(2) $Å^2$ for K, 0.0155(9) $Å^2$ for F and 0.0165(1) $Å^2$ for Te (Fig. 2b), and the occupancy of 0.990(1) for K and 0.960(5) for F. Thus, unless otherwise stated, we hereafter use the stoichiometric compositions of $K_3HTe$ and $K_3FTe$.

Most of the alkali metal rich antiperovskites $M_3HCh$ and $M_3FCh$ (M = Li, Na) reported so far have been synthesized at high pressure,[10,11] with the exception of $Na_3HTe$ and $Na_3FTe$ (unpublished data). First-principles calculations showed that the ideal cubic structure is dynamically stable at high pressure for most Na- and Li-based compounds, but at ambient pressure, many of them showed imaginary phonon modes appearing at the M and R points relevant to octahedral rotation. Here, we calculated the phonon band structures of $K_3HTe$ and $K_3FTe$ using the cubic structure at 0 and 5 GPa and found no imaginary phonon modes even under ambient pressure (Fig. 3a and b). The atom projected phonon density of states (DOS) for $K_3HTe$ indicates that the light H ion is responsible for high frequencies, whereas the heavy K and Te ions are for low frequencies. In $K_3FTe$, this tendency is less pronounced. In addition, both compounds are lower in energy at ambient pressure than the starting materials $K_2Te$ and KH/KF, suggesting that they are thermodynamically stable phases (Fig. 3c and d). These results led us to synthesize $K_3HTe$ and $K_3FTe$ under ambient pressure, and we indeed obtained the XRD patterns with identical lattice constants for both cases (Fig. S2 and S3†).

The discovery of $K_3HTe$ and $K_3FTe$ offers an opportunity to systematically compare the impact of the cations on stabiliz-

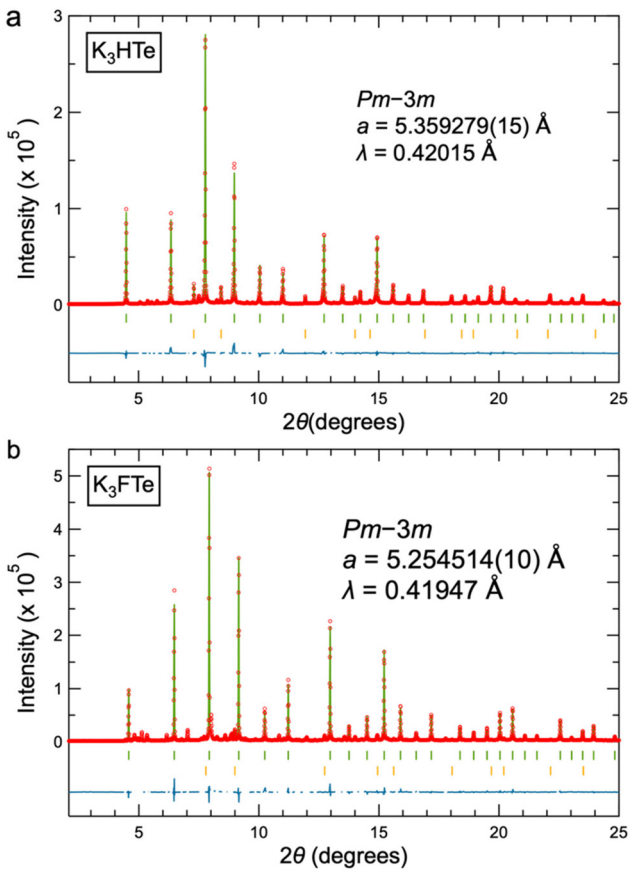


Fig. 2 Rietveld refinement of SXRD data of (a) $K_3HTe$ and (b) $K_3FTe$. The red circles, the green solid line, and the blue solid line represent the observed, calculated, and difference intensities, respectively. The upper ticks indicate the calculated Bragg reflections for (a) $K_3HTe$ and (b) $K_3FTe$, while the lower ticks for (a) KH and (b) KF. The unknown peaks are removed from the refinement.

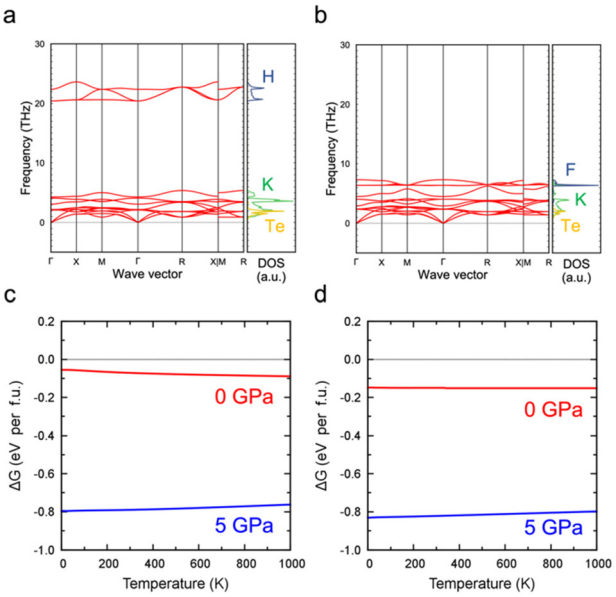


Fig. 3 Phonon band structures and partial phonon DOS of each ion of the cubic antiperovskites (a) $K_3HTe$ and (b) $K_3FTe$ at 0 GPa. The absence of imaginary phonon frequencies at the M and R points related to octahedral tilting, as found in, *e.g.*, $Na_3HS$ and $Na_3FS$,[10,11] means that both compounds are dynamically stable. The Gibbs free energy $\Delta G$ ($\Delta G = \Delta U_{internal} + P\Delta V - \Delta F_{phonon}$, $\Delta F_{phonon} = \Delta E_{ZPE} - T\Delta S_{phonon}$) of (c) $K_3HTe$ relative to that of KH + $K_2Te$ and (d) $K_3FTe$ relative to that of KF + $K_2Te$ at 0 GPa, all calculated at ambient pressure.

ation in the two sets of cubic antiperovskites, $M_3HTe$ and $M_3FTe$ (M = Li, Na, K). Fig. 4a shows the lattice parameters of cubic $M_3HTe$ and $M_3FTe$ as a function of Shannon ionic radii of the alkali metal cations, $r_M$.[27] In both systems, the lattice expands linearly with increasing $r_M$, but the slope is obviously different, with a larger value for $M_3HTe$, which suggests that this phenomenon is related to the size flexibility of hydride anions (*vs.* $F^-$).[10,28] To obtain further insights into the structural features, the obtained lattice constants were used to estimate the ionic radius of $H^-$ anions, $r_H$, where $r_H = a/2 - r_M$ ($r_{Li}$ = 0.76 Å, $r_{Na}$ = 1.02 Å, $r_K$ = 1.38 Å), as employed previously (Fig. 4b).[10] The expanded $H^-$ anion in $Na_3HTe$ compared to that in $K_3HTe$ looks reasonable because the smaller ionic radius of $Na^+$ (*vs.* $K^+$) is compensated by the larger $H^-$ anion. Following this trend, the $H^-$ radius of $Li_3HTe$ is expected to be larger than that of $Na_3HTe$. However, the opposite result, in which $H^-$ contracts, was obtained, which implies that the hydride anion is not solely responsible for stabilizing and maintaining the cubic structure.

We hence took a theoretical approach to address this issue. We estimated the Bader volume[29] for each ion using the relaxed structures at ambient pressure by first-principles calculations. In terms of the $H^-$ volume, its M dependence with a contraction at $Li_3HTe$ appears to be reproduced, as shown in Fig. 5. However, similar dependence is also found in the $F^-$ volume both qualitatively and quantitatively, with a smaller $F^-$ volume in $Li_3FTe$ than in $Na_3FTe$. Instead, a more pronounced M-dependence is seen in the tellurium anion, where the Te anion decreases its size in the order of K, Na, and Li.

The large variation in the size of the Te anion as a function of the alkali metal cations or unexpected contractions of the B-site anions in Li systems is likely related to the surface charge density of the alkali metal which, when increasing from K to Na and Li, leads to stiffer anions. We have noticed similar behaviour in lattice constants or anionic sizes in binary compounds, such as rock-salt MH[30–35] and antifluorite $M_2Te$[36–39] (Fig. S4†). Thus, the charge density of the M-site cation seems to predominantly modify the size of the Te anion to compensate for the size mismatch and preserve the cubic symmetry. Bearing in mind that Te has a high compressibility, the exceptionally small Te anion in $Li_3HTe$ is consistent with the fact that it can only be synthesized under high pressure.

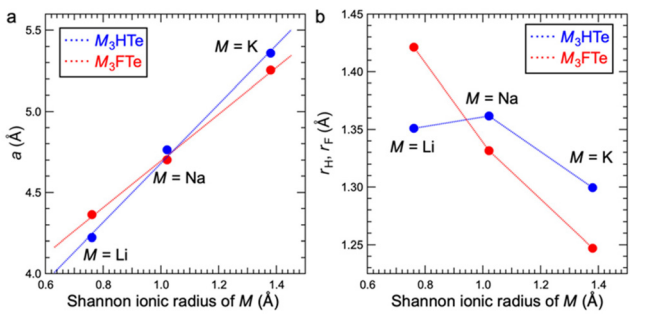


**Fig. 4** (a) The lattice parameters of (blue) $M_3HTe$ and (red) $M_3FTe$ (M = Li, Na, K).[10,11] (b) The ionic radius of $H^-$ and $F^-$, $r_H$ and $r_F$, determined from the lattice constant, where $r_H = (a - 2r_M)/2$ and $r_F = (a - 2r_M)/2$. The fixed ionic radii of 0.76 Å, 1.02 Å and 1.38 Å were used for Li, Na and K, respectively.[27] Error bars are within the circles in both figures.

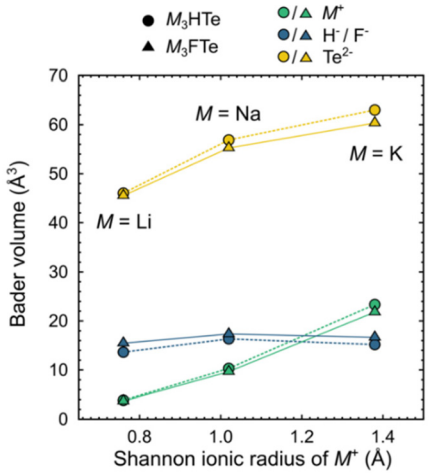


**Fig. 5** The Bader volume of the alkali metal cation (green), $H^-/F^-$ anion (blue), and $Te^{2-}$ anion (yellow) in $M_3HTe$ (circles) and $M_3FTe$ (triangles).

Since $M_3HCh$ and $M_3FCh$ (M = Li, Na; Ch = S, Se, Te) exhibit excellent lithium or sodium ion conductivity,[10,11] we performed nudged elastic band (NEB) calculations to estimate the migration energy barriers of $K^+$ transport in $K_3HTe$ and $K_3FTe$. As seen in Fig. 6, their energy barriers are comparable to those of Li-rich and Na-rich antiperovskites, as low as 265 meV and 352 meV, respectively, for the vacancy mechanism, and 76 meV and 102 meV for the interstitial dumbbell mechanism. The low migration energy barriers in K-rich antiperovskites indicate their potential as ionic conductors, once vacancies or interstitial defects are introduced by the aliovalent substitution approach, for example. $K_3HTe$ has a lower energy barrier than $K_3FTe$, which is partly due to the softer phonon

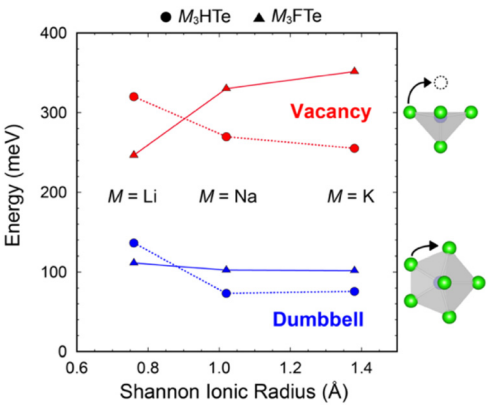


**Fig. 6** Migration energy barriers of (circles) $M_3HTe$ and (triangles) $M_3FTe$ (where M = Li, Na, K). The results of vacancy and interstitial dumbbell mechanisms are shown in red and blue, respectively. The schematics on the right side show the migration pathways of $M^+$ ions around the $HM_6/FM_6$ octahedron. The migration energy barriers of Li- and Na-rich antiperovskites are taken from ref. 10 and 11.

mode relevant to $HK_6$ octahedral rotation (Fig. S5†). Attempts to measure the $K^+$ ion conductivity of pristine and I-doped $K_3HTe$ resulted in high resistances (at least $>10^6$ Ω), which precluded proper estimation of bulk conductivities and activation energies (Fig. S6†). The large resistances may be attributed to the extremely high sensitivity of the sample surface to trace amounts of oxygen and water; thus, there is considerable room to adjust synthetic conditions in the future.

## Conclusions

We prepared two potassium-rich cubic $K_3HTe$ and $K_3FTe$ under ambient conditions, unlike the reported sodium- and lithium-rich antiperovskites $M_3HCh$ and $M_3FCh$ (M = Li, Na; Ch = S, Se, Te) stabilized under high pressure conditions. The systematic comparison of the two sets of $M_3HTe$ and $M_3FTe$ compounds, using first-principles calculations, revealed the unexpected contraction of B-site anions in Li systems and alkali metal-dependent size variation in Te anions. In perovskite oxides, the crystal structure is mainly controlled by octahedral rotations in order to compensate for the size mismatch between A, B, and O ions; thus, the cubic phase is stable only in a narrow compositional space, which could be a problem for some applications such as ionic conductivity. In contrast, the cubic structure is stable over a wide compositional space in $M_3HCh$ and $M_3FCh$. Depending on the surface charge density of the M-site cations, the Ch-site anions flexibly change their size to compensate for the size mismatch between the $BM_6$ octahedra and the Ch-site anion to maintain the cubic symmetry. The alkali metal-dependent size effects of other ions obtained in this study provide a new dimension in structural control, and thus control of physical and chemical properties, not limited to antiperovskites.

## Author contributions

K. O. and S. F. contributed equally to this work. K. O. carried out all the synthetic work and was helped by S. G. K. O., H. U. and C. T. contributed to the refinement of XRD data. S. F. and A. K. performed theoretical calculations. P. W., K. Y. and Y. U. measured the ionic conductivities. H. K. designed and coordinated this study, and contributed to all measurements and analyses.

## Conflicts of interest

There are no conflicts to declare.

## Acknowledgements

This work was supported by a Grant-in-Aid for Scientific Research on Innovative Areas "Mixed Anion" (JP16H06438, JP16H06439, and JP16H06440), a Grant-in-Aid for Specially Promoted Research "Hydrogen Ion Ceramics" (JP22H04914), a Grant-in-Aid for Scientific Research (JP22H01777, and JP23K13544), and JSPS Core-to-Core Program (A) Advanced Research Networks (JPJSCCA20200004).

## References

1 Y. Zhao and L. L. Daemen, *J. Am. Chem. Soc.*, 2012, **134**, 15042–15047.
2 X. Lü, J. W. Howard, A. Chen, J. Zhu, S. Li, G. Wu, P. Dowden, H. Xu, Y. Zhao and Q. Jia, *Adv. Sci.*, 2016, **3**, 1500359.
3 A. Emly, E. Kioupakis and A. Van Der Ven, *Chem. Mater.*, 2013, **25**, 4663–4670.
4 T. Takahashi and O. Yamamoto, *Electrochim. Acta*, 1966, **11**, 779–789.
5 K. Kamishima, T. Goto, H. Nakagawa, N. Miura, M. Ohashi, N. Mori, T. Sasaki and T. Kanomata, *Phys. Rev. B: Condens. Matter Mater. Phys.*, 2000, **63**, 24426.
6 X. Song, Z. Sun, Q. Huang, M. Rettenmayr, X. Liu, M. Seyring, G. Li, G. Rao and F. Yin, *Adv. Mater.*, 2011, **23**, 4690–4694.
7 T. He, K. A. Regan, N. Rogado, M. A. Hayward, M. K. Haas, J. S. Slusky, K. Inumara, H. W. Zandbergen and R. J. Cava, *Nature*, 2001, **411**, 54–56.
8 S. Gao, C. Tassel, S. Fujii, H. Ubukata, T. Zhu, D. Zhang, T. Broux, T. Saito, C. Zhong, E. Yoruk, K. Yamamoto, A. Kuwabara, Y. Uchimoto and H. Kageyama, *Chem. Mater.*, 2022, **34**, 6815–6823.
9 K. T. Lai, I. Antonyshyn, Y. Prots and M. Valldor, *J. Am. Chem. Soc.*, 2017, **139**, 9645–9649.
10 S. Gao, T. Broux, S. Fujii, C. Tassel, K. Yamamoto, Y. Xiao, I. Oikawa, H. Takamura, H. Ubukata, Y. Watanabe, K. Fujii, M. Yashima, A. Kuwabara, Y. Uchimoto and H. Kageyama, *Nat. Commun.*, 2021, **12**, 201.
11 S. Fujii, S. Gao, C. Tassel, T. Zhu, T. Broux, K. Okada, Y. Miyahara, A. Kuwabara and H. Kageyama, *J. Am. Chem. Soc.*, 2021, **143**, 10668–10675.
12 M. V. Goldschmidt, *Naturwissenschaften*, 1926, **14**, 477–485.
13 C. Tassel, Y. Goto, Y. Kuno, J. Hester, M. Green, Y. Kobayashi and H. Kageyama, *Angew. Chem., Int. Ed.*, 2014, **53**, 10377–10380.
14 Y. Goto, C. Tassel, Y. Noda, O. Hernandez, C. J. Pickard, M. A. Green, H. Sakaebe, N. Taguchi, Y. Uchimoto, Y. Kobayashi and H. Kageyama, *Inorg. Chem.*, 2017, **56**, 4840–4845.
15 T. Yamamoto, K. Shitara, S. Kitagawa, A. Kuwabara, M. Kuroe, K. Ishida, M. Ochi, K. Kuroki, K. Fujii, M. Yashima, C. M. Brown, H. Takatsu, C. Tassel and H. Kageyama, *Chem. Mater.*, 2018, **30**, 1566–1574.
16 C. Tassel, Y. Goto, D. Watabe, Y. Tang, H. Lu, Y. Kuno, F. Takeiri, T. Yamamoto, C. M. Brown, J. Hester, Y. Kobayashi and H. Kageyama, *Angew. Chem., Int. Ed.*, 2016, **55**, 9667–9670.

 

17 V. Petrícek, M. Dušek and L. Palatinus, *Z. Kristallogr. - Cryst. Mater.*, 2014, **229**, 345–352.
18 K. Momma and F. Izumi, *J. Appl. Crystallogr.*, 2011, **44**, 1272–1276.
19 P. E. Blöchl, *Phys. Rev. B: Condens. Matter Mater. Phys.*, 1994, **50**, 17953–17979.
20 G. Kresse and J. Hafner, *Phys. Rev. B: Condens. Matter Mater. Phys.*, 1994, **49**, 14251–14269.
21 G. Kresse and J. Furthmüller, *Phys. Rev. B: Condens. Matter Mater. Phys.*, 1996, **54**, 11169–11186.
22 J. P. Perdew, A. Ruzsinszky, G. I. Csonka, O. A. Vydrov, G. E. Scuseria, L. A. Constantin, X. Zhou and K. Burke, *Phys. Rev. Lett.*, 2008, **100**, 1–4.
23 K. Parlinski, Z. Q. Li and Y. Kawazoe, *Phys. Rev. Lett.*, 1997, **78**, 4063–4066.
24 A. Togo and I. Tanaka, *Scr. Mater.*, 2015, **108**, 1–5.
25 R. M. Pick, M. H. Cohen and R. M. Martin, *Phys. Rev. B: Solid State*, 1970, **1**, 910–920.
26 G. Mills, H. Jónsson and G. K. Schenter, *Surf. Sci.*, 1995, **324**, 305–337.
27 R. D. Shannon, *Acta Crystallogr., Sect. A: Cryst. Phys., Diffr., Theor. Gen. Crystallogr.*, 1976, **32**, 751–767.
28 H. Kageyama, K. Hayashi, K. Maeda, J. P. Attfield, Z. Hiroi, J. M. Rondinelli and K. R. Poeppelmeier, *Nat. Commun.*, 2018, **9**, 722.
29 W. Tang, E. Sanville and G. Henkelman, *J. Phys.: Condens. Matter*, 2009, **8**, 84204.
30 E. Zintl and A. Harder, *Z. Phys. Chem., Abt. B*, 1931, **14**, 265–284.
31 L. Elansari, L. Antoine, R. Janot, J. C. Gachon, J. J. Kuntz and D. Guérard, *J. Alloys Compd.*, 2001, **329**, 5–8.
32 G. S. Priyanga, A. T. A. Meenaatci, R. R. Palanichamy and K. Iyakutti, *Comput. Mater. Sci.*, 2014, **84**, 206–216.
33 N. Novaković, I. Radisavljević, D. Colognesi, S. Ostojić and N. Ivanović, *J. Phys.: Condens. Matter*, 2007, **19**, 406211.
34 H. Smithson, C. A. Marianetti, D. Morgan, A. Van Der Ven, A. Predith and G. Ceder, *Phys. Rev. B: Condens. Matter Mater. Phys.*, 2002, **66**, 1–10.
35 J. Zhang, L. Zhang, T. Cui, Y. Li, Z. He, Y. Ma and G. Zou, *Phys. Rev. B: Condens. Matter Mater. Phys.*, 2007, **75**, 1–8.
36 E. Zintl, A. Harder and B. Dauth, *Z. Elektrochem. Angew. Phys. Chem.*, 1934, **40**, 588–593.
37 H. Sommer and R. Hoppe, *Z. anorg. allg. Chem.*, 1977, **429**, 118–130.
38 Z. Souadia, A. Bouhemadou, R. Khenata and Y. Al-Douri, *Physica B: Condens. Matter*, 2017, **521**, 204–214.
39 Z. Souadia, A. Bouhemadou, S. Bin-Omran, R. Khenata, Y. Al-Douri and S. Al Essa, *J. Mol. Graphics Modell.*, 2019, **90**, 77–86.